remote sensing

MDPI

Article

Application of Multi-Temporal LiDAR for Gully Erosion Monitoring in Mediterranean Intensive Olive Groves

Sara L. Teixeira [1] and Susana Pereira [1,2,*]

[1] Centre of Studies in Geography and Spatial Planning, Faculty of Arts and Humanities, University of Porto, Via Panorâmica, s/n, 4150-564 Porto, Portugal; steixeira@letras.up.pt
[2] Centre of Geographical Studies, Institute of Geography and Spatial Planning, University of Lisbon, Rua Branca Edmée Marques, IGOT Building, 1600-276 Lisbon, Portugal
* Correspondence: sspereira@letras.up.pt

Highlights

What are the main findings?

- DoDs with high-resolution DEM allow quantifying erosion by gullies appearing in agricultural areas.
- The TNO index accurately delineates gully boundaries from multi-temporal LiDAR.

What are the implications of the main findings?

- The application of TNO and DoD provides an effective approach for detecting and quantifying gully erosion.
- This methodology enables multi-temporal monitoring, supporting regional inventory studies as well as the tracking of gully dynamics and evolutionary trends.

Abstract

Monitoring the dynamics of gullies in Mediterranean agrosystems is critical but severely limited by agricultural practices that generate continuous machinery compaction and tillage of the soil, camouflaging topographic features and disturbing erosion analyses. This study discusses strategies to quantify erosion by distinguishing natural erosion from agricultural disturbance, integrating multitemporal LiDAR data (2014, 2020, 2024) with gully inventories using orthophoto maps (2011–2022). The volumetric changes were assessed using DoD for the periods 2014–2020 and 2020–2024, and the morphometric performance of the TNO index was further validated using ROC curves in R. Both approaches performed consistently higher in detecting permanent gullies. The TNO index has proven its usefulness for semi-automated delimitation in large or low-data areas. By intersecting DoD surfaces with the gully inventory, localized erosion processes were successfully isolated from the surrounding agricultural landscape matrix. The quantified rate of erosion in the gullies refers strictly to their internal dynamics, which have been close to the natural threshold for soil formation, indicating a risk of soil degradation.

Keywords: multi-temporal; LiDAR; DEM of difference; topographic negative openness; gully erosion; agricultural landscapes

Check for updates

Academic Editor: Michele Saroli

Received: 16 September 2026
Revised: 16 October 2026
Accepted: 19 October 2026
Published: 22 October 2026

Copyright: © 2026 by the authors. Licensee MDPI, Basel, Switzerland. This article is an open access article distributed under the terms and conditions of the Creative Commons Attribution (CC BY) license.

1. Introduction

Soil is a fundamental resource for human life, sustaining agricultural production, which accounts for around 95% of the food consumed worldwide, and providing a wide

range of essential ecosystem services [1]. Monitoring soil degradation is widely recognized as a key element in achieving several SDGs, particularly those related to poverty and hunger eradication, food security, the protection of water resources, climate action, and the conservation of terrestrial and aquatic ecosystems (SDGs 1, 2, 3, 6, 11, 12, 13, 14, and 15) [2,3]. Among the various processes of soil degradation, erosion stands out as one of the most severe threats to soil health [4], with a particularly marked impact in Europe [5] and in Mediterranean regions dominated by permanent crop systems [3,6].

According to [7], approximately 23.7% of the European Union's territory has soil loss rates exceeding 1.4 t ha^{-1} yr^{-1}. This situation becomes even more serious when compared with the average rate of soil formation and natural soil renewal in Europe, estimated by Verheijen et al. [8] at only ~1.4 t ha^{-1} yr^{-1}. This concern is reflected in the EU Soil Thematic Strategy, which reinforces the urgency of integrating soil erosion as a central priority in political action [3]. Erosion rates in the hilly loess regions of Western and Central Europe are generally high, ranging between 2 and 10 t ha^{-1} yr^{-1} [9]. In Mediterranean areas, agricultural areas are estimated to experience severe water erosion and soil loss of the order of 25 Mg ha^{-1} yr^{-1}. Particularly in the region of Andalusia, where olive orchards are dominant, susceptibility to water erosion reaches critical levels, rates ranging from 6.9 Mg ha^{-1} yr^{-1} [10] to 10 Mg ha^{-1} yr^{-1} [5]. In addition, the average annual soil loss derived from field measurements of historical soil truncation ranges from 29 to 47 t ha^{-1} yr^{-1} [11]. These high rates of soil erosion result from a combination of climatic and anthropogenic factors, namely intense rainfall concentrated in short periods, often preceded by long periods of drought, and intensive agricultural practices, such as permanent olive grove cultivation [5,11].

The spatial expression of olive tree culture amplifies the relevance of this issue. In 2024, Europe accounted for more than half of global olive production (57.5%), with Spain as the global leading producer, accounting for 36.3%. Furthermore, olives were the most widely produced product in Spain (15%) [12]. The expansion of intensive olive cultivation since the 1970s has destroyed between 29% and 40% of the A and B soil horizons in some locations [11].

Soil water erosion can be assessed using multiple approaches, ranging from traditional experimental plots to intensive field-based morphological mapping [13]. However, conventional field monitoring presents significant limitations, particularly regarding its low representation of spatial–temporal variability, high economic and time costs, lack of long-term continuity, and operational constraints in accessing complex terrain [14]. Over the last two decades, HRT derived from active RS has revolutionized quantitative geomorphology, shifting the paradigm from broad-scale visual detection to volumetric quantification [15]. Among these technologies, LiDAR sensors stand out for their ability to penetrate dense vegetation canopies and provide highly accurate DEMs, effectively capturing fine-scale geomorphic changes with high-resolution spatial coverage [16].

Despite these technological advances, a critical gap remains between the available potential of HRT data and its operationalization [17] in intensive agricultural landscapes. While historical aerial photograph analysis is highly valuable for evaluating long-term 2D gully horizontal migration, it lacks the topographic depth needed to estimate 3D sediment budgets [6]. Conversely, multi-temporal LiDAR datasets offer a robust 3D framework for monitoring erosion over decadal scales [16], yet their application in active agrosystems remains limited.

This scarcity is driven by the fact that intensive agricultural systems pose specific challenges for geomorphic assessment due to continuous soil disturbance, rapid surface changes, and complex anthropogenic modifications that generate intense topographic noise, actively masking natural erosive features and disrupting micro-relief dynamics [18]. In

this context, using DoDs allows for a direct volumetric assessment of sediment loss and deposition, provided that a strict minLoD is established to filter out error propagation and sensor uncertainties [19]. However, the standalone application of DoDs frequently struggles to separate natural headcut retreat from artificial terrain leveling in intensively managed fields [17].

To overcome this limitation, morphometric indices such as TO have been increasingly applied to isolate deep, enclosed linear geometries from surrounding landscape features [13,20]. Previous studies using high-resolution DEMs demonstrated that openness is independent of light direction, thereby improving the rendering of microtopography compared to other methods [21], and proving effective for semi-automatic gully identification [22]. The application of multi-temporal DEMs and DEMs of Difference (DoDs) has been established for tracking geomorphic changes across complex, heavily modified anthropogenic landscapes, ranging from large-scale open-pit mining operations like the Bełchatów mine [23] to urbanizing environments and dynamic gully systems [24,25]. Nevertheless, the combined capability of coupling DoDs and TNO to decouple linear geomorphic signals from anthropogenic noise in intensively cultivated permanent crops remains largely untested.

In this context, the main objective of this study is to assess the capabilities and limitations of these methods, using multitemporal LiDAR data, for monitoring gully erosion dynamics influenced by Mediterranean olive cultivation practices. Specifically, this study aims to: (i) analyze the technical challenges of using multitemporal remote sensing data to quantify the morphological topographic change, (ii) evaluate the technical trade-offs and applicability of DoDs and TNO to detect and monitor gully dynamics directly under intensive agricultural management, and (iii) quantify volumetric soil loss as net topographic changes and qualitatively assess the efficiency of gully mitigation practices.

2. Materials and Methods

2.1. Study Area

The study area (Figure 1) is in Torredelcampo, Jaén, Andalusia, Spain. It is predominantly a permanent olive grove, except for a small area to the south that has been unplanted since at least 2015. It is a contributing area of approximately 0.8 km^2, which drains into a small watercourse of level 3 in the Pfafstetter hierarchy, a tributary of the Arroyo de Cadenas (level 2), which in turn is a tributary of the Arroyo Saladillo and the Arroyo Salado de Arjona. The hydrography is influenced by the relief and the presence of the A-311 road, which acts as a water divider and changes the direction of surface runoff.

The terrain is relatively flat (Figure 1), with an average altitude of 317.6 m (range: 284.4–362.2 m), an average slope of 6.2°, and a maximum slope of 59.8°, which favors the diffuse runoff.

In geological terms [26], the study area is located within the Guadalquivir Depression, bounded by the Iberian Meseta to the north and the Betic Cordillera to the south. Here, three lithological units can be found (Figure 1B): the Olistostromal unit (Tertiary, Miocene), blocks or masses of gypsum (Tertiary, Miocene), and alluvial or colluvial deposits (Quaternary).

The olistostromal unit (ranging in age from Late Langhian to Early–Middle Serravallian) exhibits a complex stratigraphic structure due to the constituent elements, which underwent displacement driven by gravitational processes. The thickness of the olistostrome in this area is approximately 500 m. Its lithology comprises materials of diverse nature—such as variously colored clays and marls, red sandstones, dolostones, and gypsum—interpreted to have originated from Triassic units. All these elements derive from the outer zones of the Betic Cordillera. Olistoliths are masses or blocks that may or may not preserve their internal structure. Gravitational processes involving debris flows and mud

flows are evident; the former can originate from the disintegration of olistoliths—indeed, the lithologies are identical, differing only in size—while the latter occur when the sliding affects more marly materials. The size of these olistoliths can range from a few meters to several hundred meters.

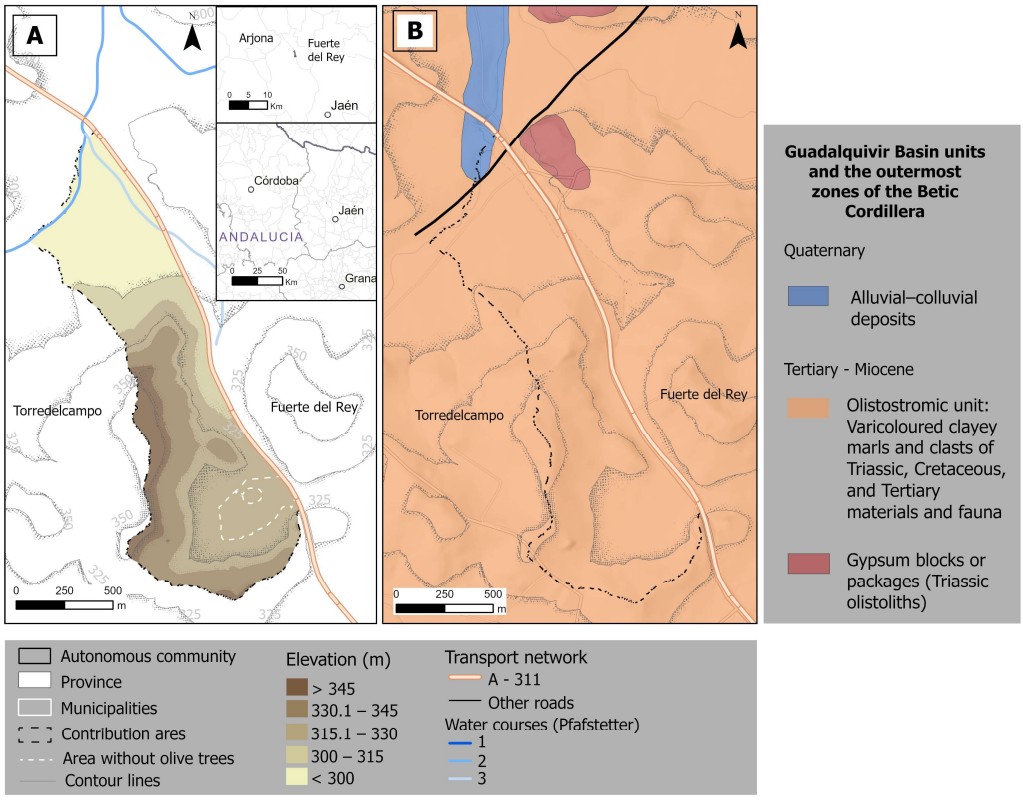


Figure 1. Study area location (**A**) and geological context (**B**). Sources: [26,27].

Blocks or masses of gypsum (Triassic olistoliths) occur in small outcrops in the study area. Alluvial or colluvial deposits (Quaternary) comprise alluvial sediments occupying the lower reaches of the current river network. Their lithological composition is silty-clayey, given that the surrounding terrain consists essentially of marl. The soils are Calcisols, loamy-clayey (30% clay, 28% sand, 42% silt), and have a basic pH.

The climate is characterised by dry, hot summers (Csa) according to the Köppen–Geiger climate classification, with low summer rainfall (average rainfall in June is 18 mm, July 2 mm, and in August is 9 mm) and rainier winters (with a maximum average of 75 mm in December) considering the data from Jaén weather station, belonging to the Spanish National Meteorological Agency (AEMET), for the period 1983–2010 (Figure 2).

Agriculture is rain-fed, with soils low in organic matter and limited biodiversity, showing signs of soil degradation, including laminar erosion, exposed roots, stoniness, and more intense erosive processes, such as rill and gullies (Figure 3).

In addition, synthetic fertilizers are used and applied to the soil and foliage. Systemic herbicide is also applied under the tree canopy.

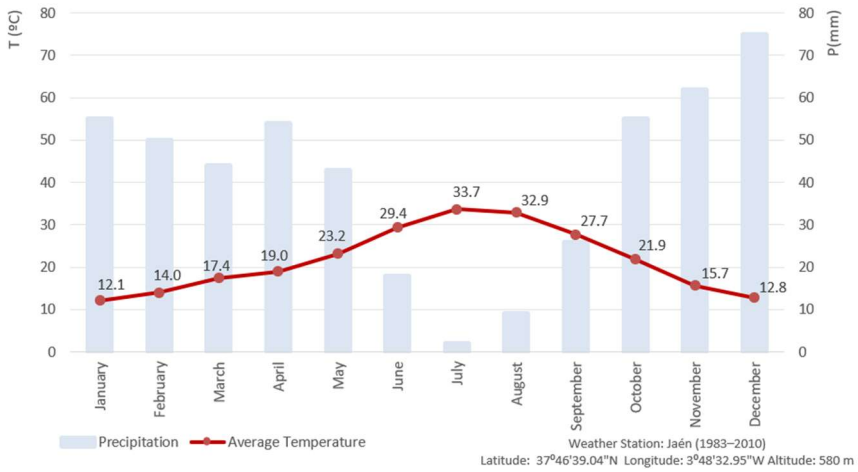


Figure 2. Monthly mean temperature and monthly mean precipitation at the Jaén weather station (AEMET, 1983–2010 period).



Figure 3. Images of typical representative gullies in the study area.

2.2. Methodologic Workflow

Altimetric data from LiDAR served as the basis for generating the DEM and was obtained from the Download Center of the National Geographic Institute. Data from 2014, 2020, and 2024 were used, with point cloud densities ranging from 0.5 to 1.5 points per m^2.

The processing of LiDAR altimetric data was structured to ensure maximum fidelity to the actual terrain surface, given that DEM spatial resolution is a critical factor in characterizing detection capacity [28]. The raw point clouds were automatically reclassified into ground and non-ground features using the Classify LAS Ground tool in ArcGIS Pro version 3.6.0, applying the Standard Ground classification method. After isolating the ground returns, the point clouds were interpolated to DEMs with a 0.75 m spatial resolution using the Triangulated Irregular Network linear interpolation, without post-processing spatial smoothing. To ensure hydrological flow-path continuity for watershed modeling only, localized sinks were processed using the Fill tool in ArcGIS Pro. This workflow was systematically replicated for the 2014, 2020, and 2024 surveys to ensure consistency and remove residual noise from vegetation and anthropogenic micro-structures.

Concurrently, active erosive features were mapped through visual interpretation and manual vectorization of IGN orthophotos (2011, 2013, 2016, 2019, and 2022) at a fixed working scale of 1:2000 (Table 1). Each gully was assigned an individual identification code for each digitized section to track morphological variations through time.

Table 1. Orthophotos characteristics information.

	2011	2013	2016	2019	2022
Spatial resolution	50 cm	50 cm	50 cm	25 cm	25 cm
Geographic system	ETRS89 (UTM 30N)	ETRS89 (UTM 30N)	ETRS89 (UTM 30N)	ETRS89 (UTM 30N)	ETRS89 (UTM 30N)
Date	2011	2013	2016	2019	2022

Morphological evolution and sediment dynamics were quantified using DoD [13,19] techniques applied to the 2014–2020 and 2020–2024 periods, enabling the calculation of net volumetric changes and annual soil loss rates.

Finally, to validate the morphometric performance of the TNO index, the continuous TNO maps derived from 2014, 2020, and 2024 LiDAR data were cross-validated against the respective post-2014, post-2020, and cumulative gully inventories (Figure 4) using ROC curves, AUC, SE, and SP.

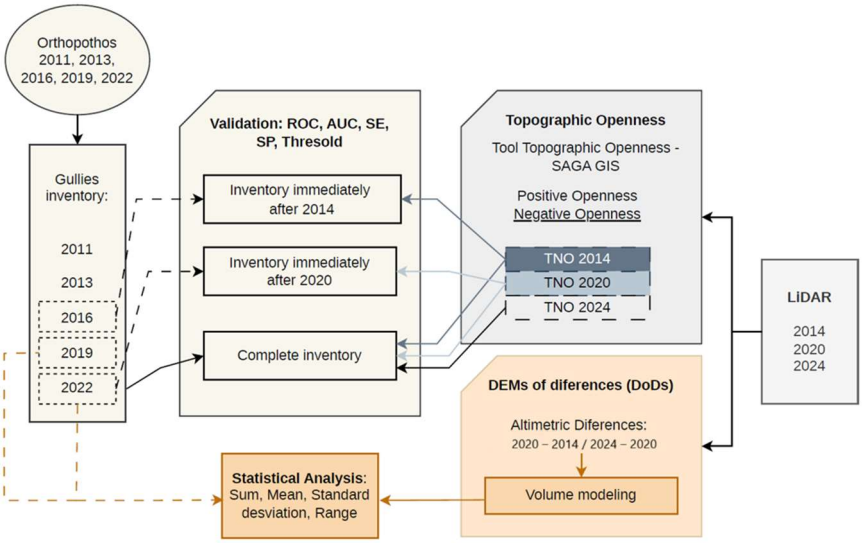


Figure 4. Methodological flowchart of the complete methodological process.

2.2.1. DEMs of Differences

The quantification of soil loss and the analysis of the evolutionary dynamics of gullies were carried out using a multitemporal approach structured into four main phases: processing altimetric differences, uncertainty analysis, spatial filtering, and statistical analysis [13,19].

To monitor morphological changes, high-resolution DEMs for 2014, 2020, and 2024 were derived from official airborne PNOA-LiDAR datasets. All point clouds were referenced to the ETRS89/UTM horizontal coordinate system, with orthometric heights calculated using the EGM2008-REDNAP geoid model. To prevent spatial resampling artifacts, exact pixel-grid alignment across temporal DEMs was ensured during spatial interpolation using the Snap Raster environment. DoDs were estimated using the Raster Calculator tool in ArcGIS Pro software to execute the following expression:

$$Altitude\ difference = Year_{recent} - Year_{older}$$

The result is a new raster dataset in which negative values indicate loss of altitude (erosion), positive values represent an increase in altitude (accumulation or deposition), and values close to zero indicate stability [13,19]. The difference in elevation between the two periods (2014–2020 and 2020–2024) was calculated, allowing the areas of erosive activity within the gullies to be isolated.

To avoid overestimating volumes and to distinguish actual geomorphological changes from digital noise, an uncertainty analysis was performed. In the absence of direct in situ GNSS control points within active gully beds, a vertical error (δ_z) of 0.20 m was assigned to the LiDAR datasets. This value corresponds to the official accuracy specifications for the baseline 2014 PNOA-LiDAR coverage and aligns with published literature that uses the same regional datasets in agricultural environments [13]. Applying this minLoD across all years provides a conservative upper-bound error estimate, as subsequent coverages (2020 and 2024) feature even higher nominal accuracies ($RMSE_z \leq 0.15$ m and $\leq$0.10 m, respectively). The uncertainty of the DoD (δ_{uDoD}) was calculated as the square root of the sum of the squares of the individual errors:

$$\delta_{uDoD} = \sqrt{(\delta_{Znew})^2 + (\delta_{Zolder})^2}$$

The resulting value of 0.28 m was applied as a filter; elevation values in the range [−0.28; +0.28] were reclassified as stable [13,19].

Finally, the raster dataset from the previous process was used to calculate the volume of lost soil. To convert volume to mass, a bulk density of 1.20 g/cm^3, with a margin of error of 0.04, was used, as reported by [29] for undisturbed loamy-clay soils in olive orchards of southern Spain, which best represent the loamy-clay soils in the study area. A conversion factor of 1 t m^{-3}/(g cm^{-3}) was applied to explicitly convert the product of volume (m^3) and bulk density (g cm^{-3}) into metric tonnes (t, where 1 g cm^{-3} = 1 t m^{-3}).

The annualized erosion rate (t ha^{-1} yr^{-1}) was calculated using the following formula:

$$Erosion\ rates = \left(\frac{Volume\ x\ Density}{Area\ analysed}\right) / Number\ of\ analysed\ years$$

This procedure was used to standardize data, enabling direct comparison with the soil renewal rate of ~1.4 t ha^{-1} yr^{-1} estimated for European soils [8].

For each sector of gullies, zonal statistical metrics for erosion values (<0) were extracted to characterize the severity and variability of the process: sum as an indicator of the total balance of soil loss in the period; mean to assess the average lowering of the gully surface; standard deviation as a measure of the spatial heterogeneity of the incision; and range to assess the difference between the extremes of depth in each sector of gullies, allowing the identification of the points that have undergone the most changes.

2.2.2. Topographic Negative Openness Calculation

The TNO specifically quantifies terrain concavity and confinement, allowing the identification of geomorphological features such as valleys, gullies, and landslides [20]. Gullies are narrow, deeply incised channels with strong local concavity and steep sidewalls [30]. This index is calculated as the average zenith angle to the surrounding surface in multiple directions within a search radius, allowing evaluation of areas where the horizon is blocked or opened by surrounding relief [20].

In this study, TNO was calculated in SAGA GIS 9.5.1 using the Topographic Openness tool, following the algorithm proposed by [20], using the standard circular neighborhood; a nominal radial search limit of 10,000 map units (meters) evaluated across 8 radial search sectors, corresponding to an angular resolution of 45° [22]. Where both large valleys and small gullies coexist, multi-scale analysis using different radius may improve feature detection [31]. The SAGA implementation calculates openness using a defined search radius (rad), generating a raster surface in which higher negative openness values represent greater topographic incision and confinement, typically associated with valley bottoms and gully thalwegs [20].

To evaluate the temporal consistency and feature-detection capability of the TNO across the multi-temporal LiDAR datasets (2014, 2020, and 2024), the previously mapped visual gully inventories (2011, 2013, 2016, 2019, and 2022) were structured into three specific temporal validation targets (Figure 4). The validation process was conducted in the R statistical environment to assess the objective reliability of the continuous TNO topographic index for discriminating between gullied (true positive) and non-gullied (true negative) terrain. In this validation architecture, the orthophoto-derived gully mappings served as the binary ground-truth target vector, while the LiDAR-derived TNO grid values acted as the continuous spatial predictor. For that, a ROC metric was calculated [32]. The diagnostic capacity of the index was evaluated using the AUC to quantify overall performance in distinguishing linear erosion. Concurrently, SE and SP were computed across the entire range of TNO values. Finally, the optimal classification threshold was defined using the Youden Index (J), maximizing the separation between active gully incisions and anthropogenic terrain noise, thus establishing an automated, statistically validated boundary for volumetric and spatial analysis.

3. Results

3.1. Gully Inventories

Gully formation exhibits a concentrated spatial pattern, represented by sectors, which is mainly dictated by local slope discontinuities (Figure 5). Sectors 1 through 3 remain persistently active over time, developing the highest depth values (>11 m) and proving to be particularly resistant to restoration measures. In contrast, sectors 4, 5, and 6 respond more favorably to interventions; their features remain small and shallow before disappearing from the inventory in later years, indicating a prolonged post-intervention recovery phase. Table 2 summarizes the gullies' characteristics (number of gullies, minimum, maximum, total, and average area; STD, and maximum estimated depth) in six sectors of the study area.

Since 2011, the mapped gully area (Figure 5) has shown an overall decreasing trend, with reductions of −2.91% between 2011 and 2013, −55.05% between 2013 and 2016, and −59.93% between 2016 and 2019. Subsequently, an approximately 9.15% increase was observed between 2019 and 2022. However, if we interpret these percentages in absolute terms, in 2011 and 2013 the gully area was around 5.000 m^2; in 2016, approximately 3.200 m^2; in 2019, about 2.000 m^2; and in 2022, 2.202 m^2. Given the large areas of change and the absence of significant changes in precipitation dynamics in the study area (Guadalquivir Hydrographic Confederation, Arenoso and Puente Nuevo stations, 2011 to 2023), these variations are mainly attributed to agricultural activity and land management practices. Such interventions tend to fragment gullies into smaller units that may later reconnect. The discontinuous nature of these interventions is likely related to difficulties in accessing deeper areas with machinery or to sporadic attempts to control gully development, resulting in a highly variable pattern of altimetric change over relatively short time periods.

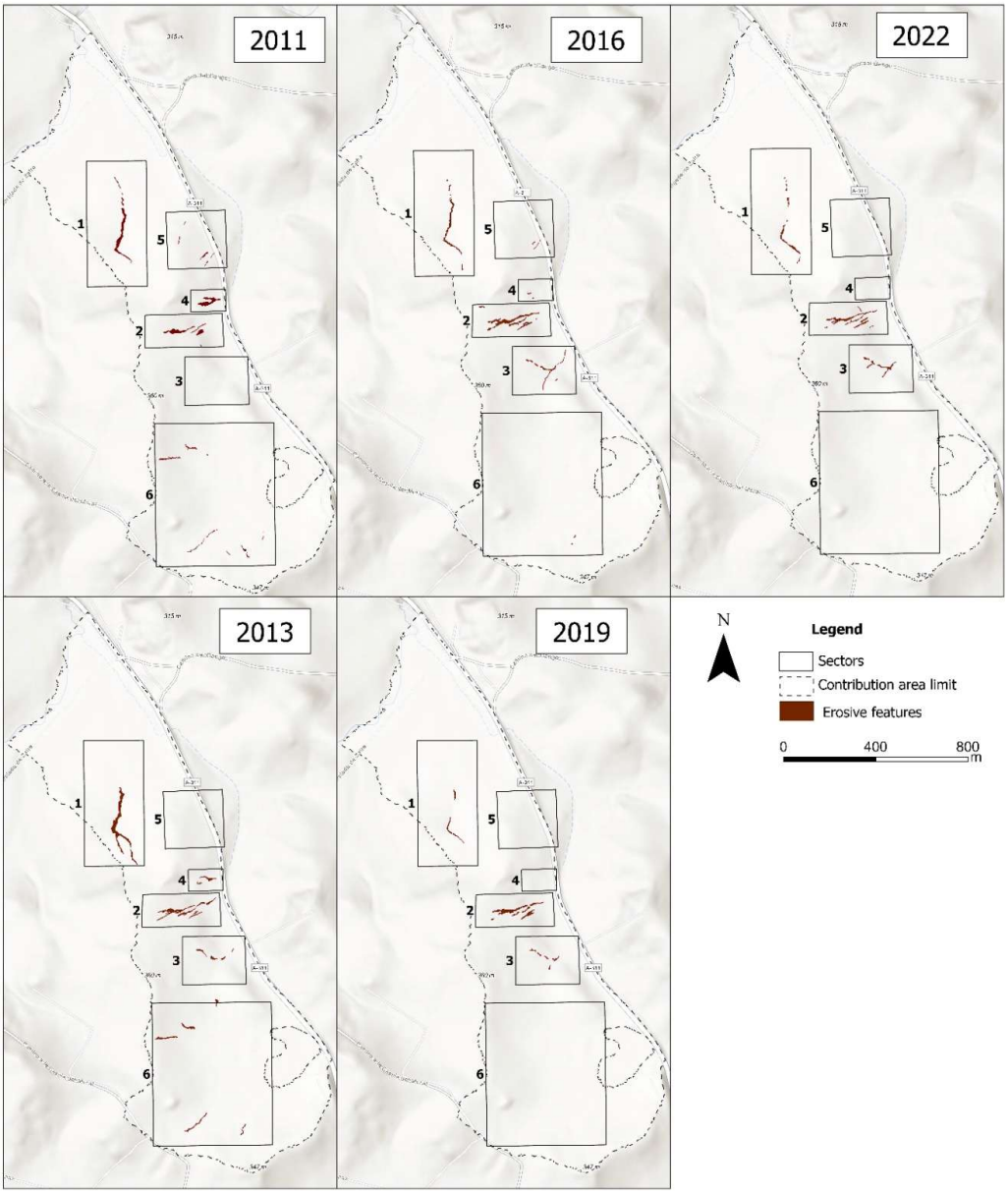


Figure 5. Gullies inventories based on orthophoto maps from 2011, 2013, 2016, 2019, and 2022 (Note: numbers correspond to sectors, see Table 2).

Table 2. Morphometric characteristics of gullies located in six sectors of the study area.

	Sector	N° of Gullies	Min. Area (m^2)	Max. Area (m^2)	Total Area (m^2)	Average Area (m^2)	Max. Estimated Depth (m)	Depth STD (m)
2011	1	5	9.42	1581.12	1829.2	365.84	7.68	4.43
	2	4	20.95	769.48	1208.15	302.04	13.90	7.16
	3	-	-	-	-	-	-	-
	4	1	-	-	857.26	-	6.01	2.95
	5	5	30.11	129.26	287.19	57.44	6.16	3.84
	6	7	19.66	258.32	923.92	131.99	9.21	6.82

Table 2. *Cont.*

	Sector	N° of Gullies	Min. Area (m^2)	Max. Area (m^2)	Total Area (m^2)	Average Area (m^2)	Max. Estimated Depth (m)	Depth STD (m)
2013	1	2	11.87	115.03	2208.38	1104,19	9.36	6.59
	2	6	39.66	772.96	1282.03	213.67	18.31	8.39
	3	4	11.87	115.03	304.51	76.13	8.94	4.66
	4	2	49.15	213.40	262.38	131.19	5.14	2.83
	5	-	-	-	-	-	-	-
	6	6	28.85	255.75	903.83	150.64	8.09	6.75
2016	1	7	4.35	766.86	944.49	134.93	8.78	5.74
	2	6	4.04	1144.82	1669.01	278.17	17.74	8.37
	3	6	17.14	293.74	484.63	80.77	9.03	4.88
	4	2	6.84	24.39	31.21	15.61	1.71	1.02
	5	3	2.33	24.08	46.19	15.40	2.73	1.18
	6	2	7.49	16.70	24.18	12.09	0.84	0.74
2019	1	3	80.27	186.40	384.41	128.14	6.69	4.72
	2	6	32.64	79.80	1380.11	230.02	16.20	7.51
	3	5	28.76	750.66	236.19	47.24	6.65	4.27
	4	-	-	-	-	-	-	-
	5	-	-	-	-	-	-	-
	6	-	-	-	-	-	-	-
2022	1	8	6.11	480.33	659.42	82.43	11.16	6.44
	2	7	8.94	651.78	1046.52	149.50	16.01	7.38
	3	4	49.91	302.64	473.79	118.45	7.02	4.38
	4	1	-	-	22.52	-	1.29	0.73
	5	-	-	-	-		-	-
	6	-	-	-	-		-	-

3.2. DEMs of Difference

The net soil loss rate was quantified strictly considering the inner footprint of the gully boundaries. The results revealed net soil loss values of 0.759 t ha^{-1} yr^{-1} for the 2014–2020 period and 1.035 t ha^{-1} yr^{-1} for the 2020–2024 period within the active gully channels. When contextualized at the catchment scale (4.076 in 2014–2020 and 2.862 in 2020–2024), these rates indicate degradation, exceeding the average natural soil renewal rate for Mediterranean environments (1.4 t ha^{-1} yr^{-1}). This confirms that the study area is degraded by concentrated water erosion, with permanent gullies actively evolving across sectors 1, 2, 3, and 4 (Figure 6).

The widening of ravines in Mediterranean regions is usually associated with prolonged drought followed by intense, concentrated storm events, which may explain the rapid expansion of the erosion system observed between 2014 and 2024. However, the climate factor alone is insufficient to explain the observed dynamics. A comparison with the history of gullies confirms the relevance of other conditioning factors, namely agricultural land management (e.g., tillage, soil compaction), which often fragments gullies into small units that tend to regroup over time, as illustrated by the emergence of gully 4, which was not identified in 2019.

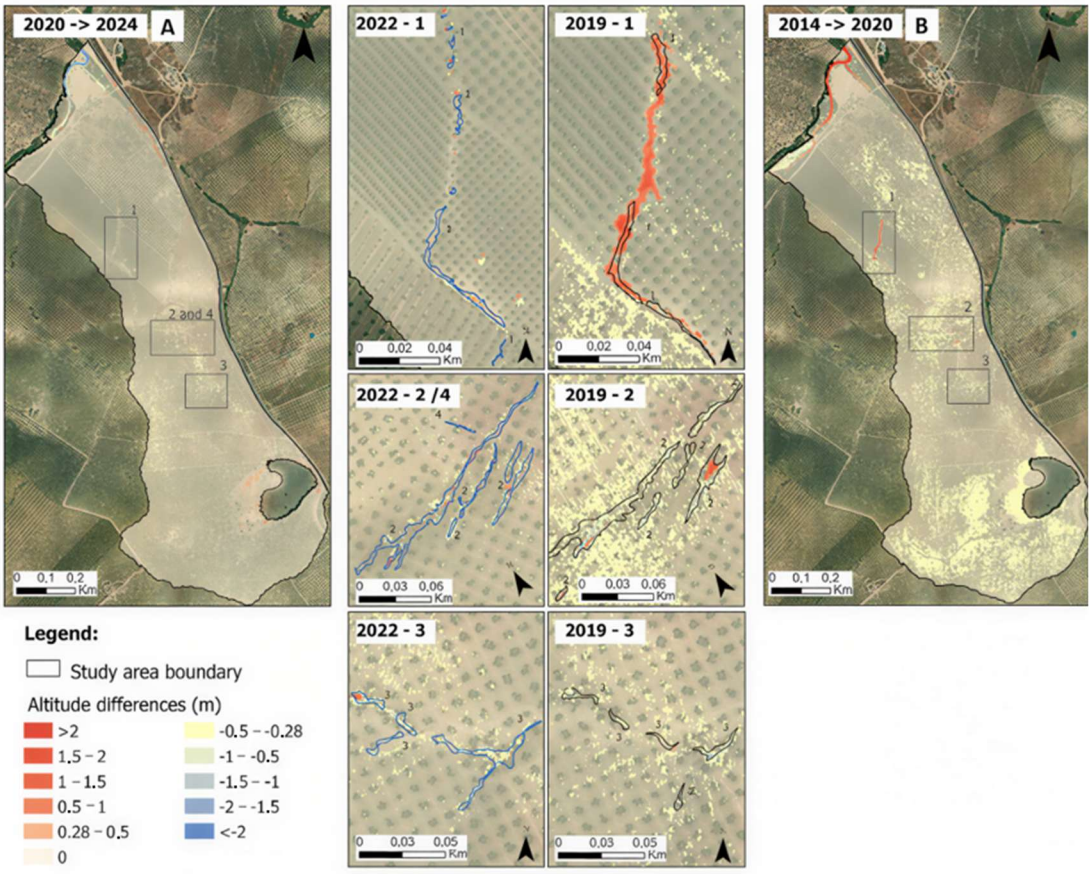


Figure 6. Altitude differences in the gullied area sectors between 2020 and 2024 (**A**) and 2014 and 2020 (**B**), with central panels showing detailed gully boundary sector evolution derived from orthophoto map photo-interpretation in 2019 and 2022. (Note: numbers correspond to sectors 1, 2, 3, and 4, see Table 2 and Figure 5).

In Table 3, sector 3 stands out as having the highest soil loss in the first period (−0.357 t ha^{-1} yr^{-1}) and the second-highest in the second period (−0.390 t ha^{-1} yr^{-1}), indicating persistent erosion. In contrast, sector 2 is the only one in which soil loss decreased, from −0.065 t ha^{-1} yr^{-1} (2014–2020) to −0.022 t ha^{-1} yr^{-1} (2020–2024).

Table 3. Evolutionary dynamics of soil loss in gullied areas between 2014 and 2024.

		Sector					
Period		**1**	**2**	**3**	**4**	**Total Gully Erosion**	**Total Erosion in the Contribution Area**
2014–2020	Sum (t ha^{-1} yr^{-1})	−0.005	−0.065	−0.357	-	−0.759	−4.076
2020–2024		−0.056	−0.022	−0.390	−0.171	−1.035	−2.862
2014–2020	Mean (m)	−0.009	−0.206	−0.175	-	−0.176	−0.137
2020–2024		−0.048	−0.096	−0.186	−0.096	−0.087	−0.064
2014–2020	Range (m)	0.329	0.798	0.529	-	1.214	1.439
2020–2024		0.212	0.410	0.663	0.199	0.903	2.056
2014–2020	Standard deviation (m)	0.039	0.167	0.141	-	0.195	0.071
2020–2024		0.044	0.085	0.148	0.046	1.118	0.088

In turn, Table 3 shows a general increase in the elevation standard deviation in the period 2020–2024 (e.g., in sector 1, from 0.039 m to 0.044 m) suggests that the gullies are at a more advanced stage of development, with more uniform erosion processes, probably resulting from the reduction of easily erodible material and the stabilization of already established incisions, which reflects less altimetric variability.

Once more, the direct influence of anthropogenic interventions is particularly evident in the analysis of gully evolution. While some sections of the gullies were filled with sediments, resulting in local altimetric increases (Figure 6), others remained exposed and highly susceptible to water erosion. Nevertheless, the sum of the accumulated altimetric differences proved particularly effective in identifying the most critical erosive sectors, with sector 3 highlighted.

3.3. Topographic Negative Openness

The TNO data (in radians) are very close over the years (Figure 7); however, the minimum value decreased from 0.88 in 2014 to 0.87 in 2020, then increased to 0.9 in 2024. The maximum value remained relatively stable between 2014 and 2020, at around 1.58, but increased to 1.73 in 2024. Thus, in the first two years, the maximum value aligns with the theoretical value for flat surfaces, approximately $\pi/2$ ($\approx$1.57) [20], whereas in 2024 it exceeds that value. This can be explained by the presence of more pronounced convex shapes or by the model's greater roughness, suggesting changes in the micro-relief.

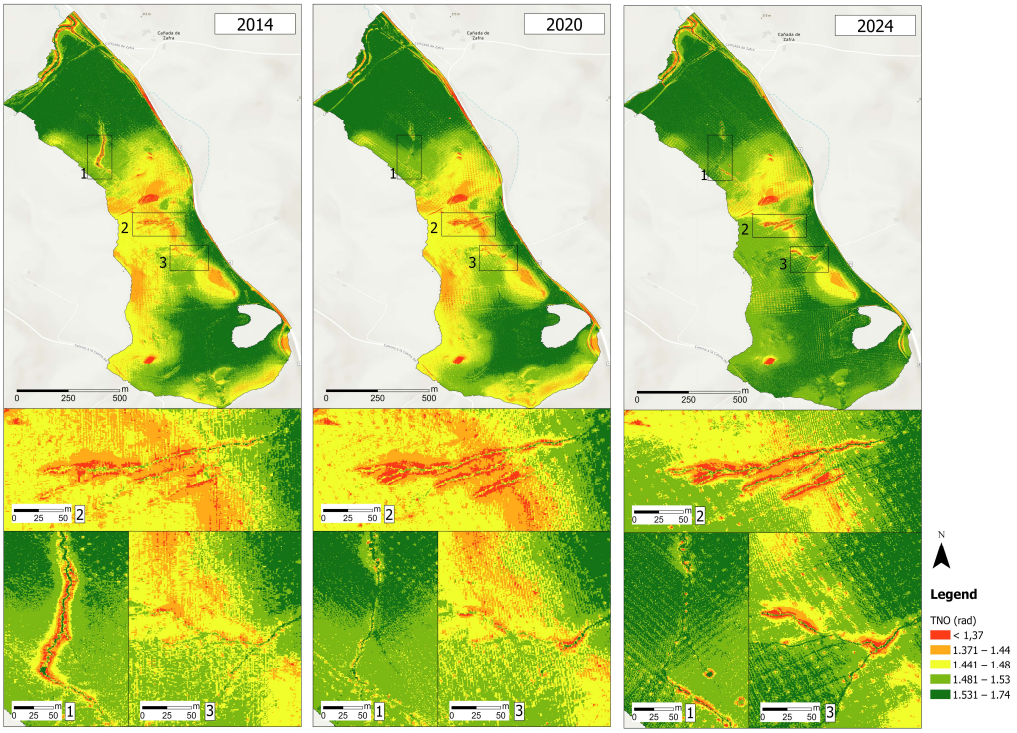


Figure 7. Topographic Negative Openness (2014, 2020, and 2024). (Note: numbers correspond to sectors 1, 2, and 3, see Table 2 and Figure 5).

The analysis of Figure 7 also reveals areas of the basin with high stability over time (TNO > 1.52), indicating flatter surfaces. The sites with the lowest values, indicating the presence of gullies (Sectors A, B, C), are surrounded by TNO values below $\approx$1.57, revealing greater topographic incision.

In TNO, low values (usually below 1.5 rad) highlight pronounced concave features, particularly gully headcuts and incision channels, which serve as structural indicators for gully extraction before subsequent validation against inventories (Figure 7). ROC

curves allow the evaluation of TNO performance in highlighting linear incision zones, providing a robust measure of its ability to guide feature detection between stable slopes and active channels. However, it is important to note that the use of TNO should always be validated by subsequent inventories conducted immediately after, under the same climatic conditions, land use, and agricultural practices. Otherwise, its predictive capacity falls below acceptable levels because the index is highly sensitive to changes in surface roughness that may not be related to active linear erosion processes.

When comparing the ROC AUC of the TNO index against the gully inventory compiled immediately after the modeling date (Figure 8A), the 2014 model exhibits the highest performance (AUC = 0.81). Conversely, the validation against the cumulative historical gully inventory (Figure 8B) yields slightly lower yet acceptable-to-good predictive performance, with 2024 achieving the highest AUC (0.790), followed by 2014 (AUC = 0.729) and 2020 (AUC = 0.665). Across all tested scenarios, TNO performs better than random classification. However, performance varies over time due to the dynamic nature of the agricultural landscape, in which tillage practices [6,11] and fluctuating hydrological conditions alter surface roughness.

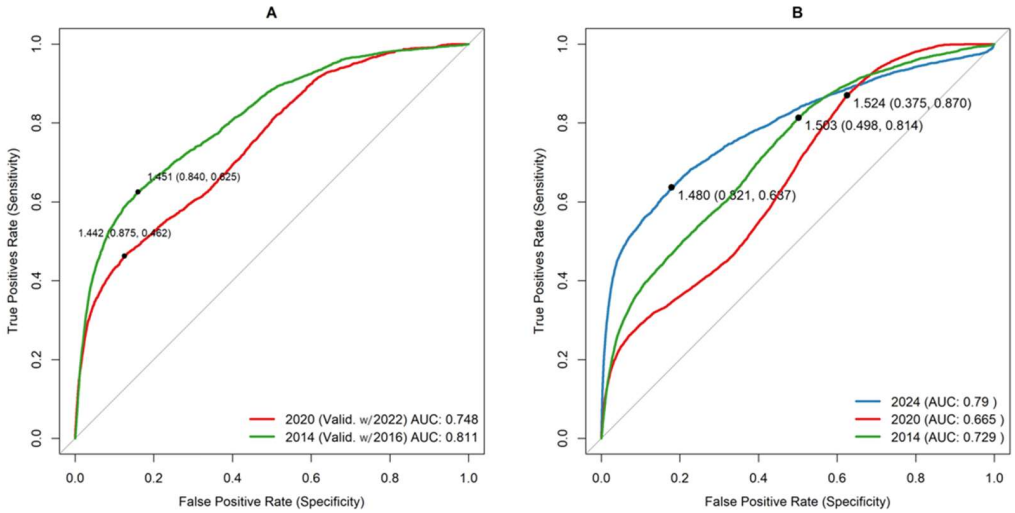


Figure 8. ROC curves and AUC values of the TNO using the gully inventory after the LiDAR acquisition date (**A**) and the historical gully inventory (**B**).

The analysis of optimal thresholds, defined by the optimal balance between Se and Sp, demonstrates consistency across all years, ranging from 1.442 to 1.524 rad (Figure 8). This consistency confirms that a cut-off value near 1.5 rad is a robust indicator for identifying structural incision zones. Nonetheless, because this threshold lies close to the theoretical value for flat surfaces (1.57 rad) [20], it inevitably captures minor microtopographic concavities, leading to potential confusion with rill erosion, agricultural furrows, roadside ditches, or DEM interpolation artifacts. For instance, in Figure 8A, the 2020 model exhibits high sensitivity (0.87) but low specificity (0.46), indicating strong detection of active incisions at the expense of a high false-positive rate. In contrast, the 2014 model achieves a balanced compromise between sensitivity (0.84) and specificity (0.62), providing superior discrimination between stable terrain and active gullies. From a geomorphological perspective, these results confirm that the TNO index effectively captures the morphometric signature of linear erosion. Overall, immediate post-event validations provide the highest predictive skill (AUC up to 0.81), whereas evaluations against inventories after the LiDAR acquisition yields acceptable average performance (AUC ~0.665 for the 2020 inventory and ~0.79 for the 2014 inventory) but lower sensitivity, underscoring the dynamic influence of land management on gully preservation.

From a geomorphological perspective, these results indicate that the TNO index is a relevant morphometric tool for highlighting gully headcuts and channel thalwegs in this study area, effectively capturing the topographic signature of linear incision processes to support semi-automated feature mapping. It should also be noted that validations carried out on the inventory after the modeled years show better AUC values, around 0.78; however, sensitivity tends to be lower, highlighting the limitations inherent in the availability of validation data.

4. Discussion

4.1. Methodological Challenges and Validation in Agricultural Areas

Despite the increasing availability of airborne LiDAR data, the application of high-resolution multitemporal LiDAR-derived products, such as TNO and DoDs, remains scarce in intensively cultivated catchments [21,22]. Most existing studies investigating gully erosion using these techniques have focused on less disturbed landscapes, generally relying on coarser spatial resolutions and lacking a multitemporal perspective [21,22,31].

This gap in the literature is largely due to the limited availability of repeated, high-resolution topographic datasets required for DoD analyses, as the logistical and financial costs of acquiring multitemporal elevation data frequently constrain long-term erosion monitoring. Nevertheless, the results of the present study demonstrate that, once these data limitations are overcome, multitemporal LiDAR methodologies perform well. The integrated approach proved effective not only in detecting established permanent gullies but also in identifying ephemeral linear incisions, even within a highly dynamic agricultural landscape subject to frequent soil disturbance.

However, implementing and validating these algorithms in actively cultivated environments reveals a clear geomorphological paradox. Tillage operations and the repeated passage of agricultural machinery cause rapid non-geomorphic surface changes and pronounced microtopographic roughness [17,33]. Although a detailed spatial resolution (0.75 m) is essential for improving volumetric quantification through DoD analysis, it simultaneously captures transient anthropogenic features such as tillage furrows, wheel tracks, and localized soil compaction. Since these temporary modifications do not represent long-term geomorphic change, morphological budgets become sensitive to structural noise [18,34].

TNO proved particularly effective at enhancing concave landforms and facilitating the semi-automated identification of gully headcuts and incision lines, as also reported by Lv et al. [21]. However, because the surrounding landscape is predominantly characterized by gently sloping agricultural terrain with limited local relief, the mathematical contrast generated by topographic openness naturally decreases across these flatter surfaces, thereby reducing the index's discriminative power [20]. Consequently, confusion between non-erosive agricultural disturbances (e.g., tractor wheel tracks or tillage marks) and genuine erosional features increases, leading to higher false-positive rates and highlighting the need for expert manual validation during vectorization.

In contrast, the morphological signature of permanent gullies, characterized by deep and continuous linear incisions, remains well above the background microtopographic noise. Consequently, by incorporating an inventory of existing gullies delineated from orthophotos with a spatial resolution finer than the DEM, it was possible to successfully isolate consolidated geomorphic features from temporary anthropogenic roughness. This improved the robustness of permanent gully monitoring and reduced false detections [13,19].

4.2. Sensor Limitation, Error Propagation, and Uncertainty

A robust quantification of soil loss using remote sensing requires a transparent assessment of sensor limitations and error propagation. In this study, the elevation data obtained from the IGN had point densities ranging between 0.5 and 1.5 points m^2, constraining the final raster resolution to 0.75 m and limiting the accurate representation of small erosional features. This spatial resolution is highly effective for characterizing permanent channels but also acts as a spatial filter, inevitably smoothing microtopographic features. Consequently, the earliest stages of linear erosion (incipient rills) are systematically underrepresented, as their dimensions fall below the sensor's detection threshold. For this reason, the present study focused on soil loss associated with gully erosion.

Furthermore, the morphometric changes derived from the DoDs are intrinsically constrained by the established minLoD = 0.28 m. This threshold is mathematically essential to prevent digital noise, soil compaction effects, or artificial surface roughness from being misinterpreted as genuine geomorphic change [19]. However, it also creates a critical omission threshold at gully headcuts. Geomorphologically significant processes, such as headcut retreat or bank failures with depths below 28 cm, are classified as "stable" by the filtering procedure. This conservative constraint implies that the reported erosion rates should be interpreted as minimum estimates, since part of the initial linear erosion is removed during error propagation.

Finally, an important physical limitation concerns the conversion of volumetric changes (m^3) into estimates of sediment mass. The adoption of a uniform bulk density of 1.20 g cm^{-3} derived from undisturbed soils, although representative of Mediterranean clay-loam soils [29], introduces a structural simplification into the sediment budget. In actively incising gullies, bulk density is rarely spatially homogeneous. Gully floors commonly undergo cyclic compaction due to concentrated runoff, whereas channel banks experience progressive loosening, structural weakening, and reduced cohesion before failure through mass wasting and gravitational collapse [35]. This spatial heterogeneity introduces inherent uncertainty into absolute sediment mass calculations, highlighting a common limitation of studies that rely exclusively on topographic differencing without comprehensive, spatially distributed field measurements [36].

4.3. Sediment Balance and Soil Conservation Strategies

The average net soil loss rate documented during the monitored decade (~0.759 to ~1.035 t ha^{-1} yr^{-1}), when contrasted with the average natural soil formation rate reported for European Mediterranean environments (1.4 t ha^{-1} yr^{-1}) [8]. Although long-term erosion rates exceeding 1.2 t ha^{-1} yr^{-1} are typically required to induce an immediate collapse in agricultural productivity [11], the continuous net deficit documented between 2014 and 2024 represents a progressive depletion of the topsoil matrix that steadily compromises agricultural sustainability. A deeper analysis of the multi-temporal DoD results reveals a highly connected sediment network. This network is strongly controlled geomorphologically by slopes exceeding 15° and low TWI (<4) values, indicating that active linear incision processes are dominant near the upper hillslopes and basin boundaries. In intensive agricultural systems, this spatial pattern can be accelerated by heavy machinery traffic, which, in our study area, is further aggravated by the presence of surface soil crusts. This crusting drastically reduces infiltration capacity and increases the erosive action of surface runoff. This mechanism promotes a faster transition from diffuse rill erosion to gully evolution [35], consequently worsening the diagnostic outlook of the studied area.

Long-term monitoring indicates sporadic attempts at mechanical gully infilling. However, the rapid reappearance of features such as Gully 4, which was absent in 2019 due to tillage but re-emerged in 2022, demonstrates that mechanical infilling provides only tempo-

rary stabilization. Conversely, it creates a highly unconsolidated soil structure precisely within the concentrated flow path. During subsequent intense rainfall events, runoff can re-excavate the inherited channel, demonstrating that interventions without hydrological control are inefficient.

Thus, multi-temporal LiDAR datasets provide an objective and easily interpretable spatial diagnosis to transition from reactive remediation to a dynamics-based process mitigation. Instead of unthinkingly infilling channels, the spatial convergence zones identified by the TNO and the critical erosion hotspots mapped by the DoD allow us to conclude that mitigation measures must prioritize reducing hydrological connectivity and stabilizing slopes at the exact points where steep gradients and high runoff concentrations converge.

The implementation of permanent vegetative cover along structural flow lines (grassed waterways) [37], the strategic construction of small sediment retention dams (check-dams) upstream of active headcuts [38], and drainage control along agricultural access roads [39] represent the most efficient strategies to alter the basin's energy balance and mitigate degradation in vulnerable Mediterranean agricultural landscapes.

5. Conclusions

Ultimately, this study confirms that a workflow based on multitemporal LiDAR datasets provides a useful framework for systematically implementing targeted mitigation strategies for water-erosion processes concentrated in vulnerable Mediterranean agricultural ecosystems. The main conclusions address the three central objectives established in this investigation.

Firstly, our results confirm that the TNO index demonstrates good potential performance in identifying linear incision zones within intensively cultivated olive groves. Validation using ROC curves produced AUC values higher than random classification, along with robust specificity metrics. This reveals that TNO has good potential as an effective morphometric support for pinpointing gully headcuts and channel axes, enabling efficient semi-automated vectorization and mapping, especially when historical inventories are unavailable, data acquisition is limited, or in agricultural contexts.

Secondly, this morphometric detection proved to be complementary when combined with DoDs techniques. By intersecting the DoD volumetric surfaces with the independent gully inventory, the specific erosion and deposition processes associated with these linear forms were delineated from the surrounding landscape matrix. This methodological integration helps reduce agricultural noise, providing a refined estimate of the actual soil erosion loss from gullies.

Thirdly, although our findings confirm that these methodologies are effective, affordable, and time-efficient, a geographical gap remains, limiting the comprehensive discussion of their long-term behavior in agricultural landscapes with different permanent cropping systems under varying climatic, lithological, and soil management regimes.

Author Contributions: Conceptualization, S.L.T. and S.P.; methodology, S.L.T. and S.P.; software, S.L.T.; validation, S.L.T. and S.P.; formal analysis, S.L.T.; investigation, S.L.T. and S.P.; resources, S.L.T. and S.P.; data curation, S.L.T.; writing—original draft preparation, S.L.T.; writing—review and editing, S.L.T. and S.P.; visualization, S.L.T. and S.P.; supervision, S.P.; project administration, S.P. All authors have read and agreed to the published version of the manuscript.

Funding: This work was funded by the LivingSoiLL project "Healthy Soil to Permanent Crops Living Labs", Horizon Europe, funded by the European Commission under the Grant Agreement 101157502 under the EU Mission "A Soil Deal for Europe". This work was funded by national funds through FCT—Foundation for Science and Technology, I.P., under the project UIDB/04084/2025 (https://doi.org/10.54499/UID/04084/2025)—Centre for Studies in Geography and Spatial Planning | FLUP.

Data Availability Statement: The dataset used in this study includes publicly available spatial data. The Orthophotos are available from the *Plan Nacional de Ortofotografía Aérea* (PNOA) via https://pnoa.ign.es (accessed on 18 October 2026). The LiDAR data were obtained from the Centro de Descargas del Instituto Geográfico Nacional (CNIG) at https://centrodedescargas.cnig.es (accessed on 18 October 2026).

Acknowledgments: The authors would like to thank Julio Antonio Calero González for providing the photographs of the gullies in the study area.

Conflicts of Interest: The authors declare no conflicts of interest.

Abbreviations

2D	Two-dimensional
3D	Three-dimensional
AUC	Area Under the Curve
DEM	Digital Elevation Models
DoDs	DEMs of Differences
HRT	High-Resolution Topography
LiDAR	Light Detection and Ranging
minLoD	Minimum Level of Detection
ROC	Receiver Operating Characteristic
RS	Remote Sensing
SDGs	Sustainable Development Goals
SE	Sensitivity
SP	Specificity
TNO	Topographic Negative Openness
TO	Topographic Openness
TWI	Topographic Wetness Index

References

1. Borrelli, P.; Robinson, D.A.; Panagos, P.; Lugato, E.; Yang, J.E.; Alewell, C.; Wuepper, D.; Montanarella, L.; Ballabio, C. Land use and climate change impacts on global soil erosion by water (2015–2070). *Proc. Natl. Acad. Sci. USA* **2020**, *117*, 21994–22001. [CrossRef] [PubMed]
2. Wang, J.; Zhen, J.; Hu, W.; Chen, S.; Lizaga, I.; Zeraatpisheh, M.; Yang, X. Remote sensing of soil degradation: Progress and perspective. *Int. Soil Water Conserv. Res.* **2023**, *11*, 429–454. [CrossRef]
3. Ferreira, C.S.S.; Seifollahi-Aghmiuni, S.; Destouni, G.; Ghajarnia, N.; Kalantari, Z. Soil degradation in the European Mediterranean region: Processes, status and consequences. *Sci. Total Environ.* **2022**, *805*, 150106. [CrossRef] [PubMed]
4. Arabameri, A.; Pradhan, B.; Rezaei, K.; Conoscenti, C. Gully erosion susceptibility mapping using GIS-based multi-criteria decision analysis techniques. *Catena* **2019**, *180*, 282–297. [CrossRef]
5. Espejo-Pérez, A.J.; Rodríguez-Lizana, A.; Ordóñez, R.; Giráldez, J.V. Soil loss and runoff reduction in olive-tree dry-farming with cover crops. *Soil Sci. Soc. Am. J.* **2013**, *77*, 2140–2148. [CrossRef]
6. Lima, F.; Blanco-Sepúlveda, R.; Calle, M.; Andújar, D. Reconstruction of historical soil surfaces and estimation of soil erosion rates with mound measurements and UAV photogrammetry in Mediterranean olive groves. *Geoderma* **2023**, *440*, 116708. [CrossRef]
7. Panagos, P.; Borrelli, P.; Poesen, J.; Ballabio, C.; Lugato, E.; Meusburger, K.; Montanarella, L.; Alewell, C. The new assessment of soil loss by water erosion in Europe. *Environ. Sci. Policy* **2015**, *54*, 438–447. [CrossRef]
8. Verheijen, F.G.A.; Jones, R.J.A.; Rickson, R.J.; Smith, C.J. Tolerable versus actual soil erosion rates in Europe. *Earth-Sci. Rev.* **2009**, *94*, 23–38. [CrossRef]
9. Cerdan, O.; Govers, G.; Le Bissonnais, Y.; Van Oost, K.; Poesen, J.; Saby, N.; Gobin, A.; Vacca, A.; Quinton, J.; Auerswald, K.; et al. Rates and spatial variations of soil erosion in Europe: A study based on erosion plot data. *Geomorphology* **2010**, *122*, 167–177. [CrossRef]
10. Gómez, J.A.; Sobrinho, T.A.; Giráldez, J.V.; Fereres, E. Soil management effects on runoff, erosion and soil properties in an olive grove of Southern Spain. *Soil Tillage Res.* **2009**, *102*, 5–13. [CrossRef]
11. Vanwalleghem, T.; Amate, J.I.; de Molina, M.G.; Fernández, D.S.; Gómez, J.A. Quantifying the effect of historical soil management on soil erosion rates in Mediterranean olive orchards. *Agric. Ecosyst. Environ.* **2011**, *142*, 341–351. [CrossRef]

12. FAO. *FAOSTAT Statistical Database*; FAO: Rome, Italy, 2024.
13. Fernández, T.; Pérez-García, J.L.; Gómez-López, J.M.; Cardenal, J.; Calero, J.; Sánchez-Gómez, M.; Delgado, J.; Tovar-Pescador, J. Multitemporal analysis of gully erosion in olive groves by means of digital elevation models obtained with aerial photogrammetric and LiDAR data. *ISPRS Int. J. Geo-Inf.* **2020**, *9*, 260. [CrossRef]
14. Beniaich, A.; Silva, M.L.N.; Guimarães, D.V.; Avalos, F.A.P.; Terra, F.S.; Menezes, M.D.; Avanzi, J.C.; Cândido, B.M. UAV-based vegetation monitoring for assessing the impact of soil loss in olive orchards in Brazil. *Geoderma Reg.* **2022**, *30*, e00543. [CrossRef]
15. Tarolli, P. High-resolution topography for geomorphological studies. *Geomorphology* **2014**, *214*, 111–134. [CrossRef]
16. Starek, M.J.; Mitasova, H.; Hardin, E.; Weaver, K.; Overton, M.; Harmon, R.S. Modeling and analysis of landscape evolution using airborne, terrestrial, and laboratory laser scanning. *Geosphere* **2011**, *7*, 1340–1356. [CrossRef]
17. Ehrhardt, A.; Deumlich, D.; Gerke, H.H. Soil surface micro-topography by Structure-from-Motion photogrammetry for monitoring density and erosion dynamics. *Front. Environ. Sci.* **2022**, *9*, 737702. [CrossRef]
18. Hänsel, P.; Schindewolf, M.; Eltner, A.; Kaiser, A.; Schmidt, J. Feasibility of high-resolution soil erosion measurements by means of rainfall simulations and SfM photogrammetry. *Hydrology* **2016**, *3*, 38. [CrossRef]
19. Wheaton, J.M.; Brasington, J.; Darby, S.E.; Sear, D.A. Accounting for uncertainty in DEMs from repeat topographic surveys: Improved sediment budgets. *Earth Surf. Process. Landf.* **2009**, *35*, 136–156. [CrossRef]
20. Yokoyama, R.; Shirasawa, M.; Pike, R.J. Visualizing topography by openness: A new application of image processing to digital elevation models. *Photogramm. Eng. Remote Sens.* **2002**, *68*, 257–265.
21. Lv, J.; Lu, C.; Ye, M.; Long, Y.; Li, W.; Yang, M. Enhanced landslide visualization and trace identification using LiDAR-derived DEM. *Sensors* **2025**, *25*, 4391. [CrossRef] [PubMed]
22. Codru, I.-C.; Niacsu, L.; Enea, A.; Bou-imajjane, L. Inventory and semi-automatic gully extraction using LiDAR and topographic openness-Case study: Covurlui Plateau, Eastern Romania. *Land* **2023**, *12*, 1199. [CrossRef]
23. Dai, W.; Yang, X.; Na, J.; Li, J.; Brus, D.; Xiong, L.; Tang, G.; Huang, X. Effects of DEM resolution on the accuracy of gully maps in loess hilly areas. *Catena* **2019**, *177*, 114–125. [CrossRef]
24. Jaskulski, M.; Nowak, T. Transformations of Landscape Topography of the Bełchatów Coal Mine (Central Poland) and the Surrounding Area Based on DEM Analysis. *ISPRS Int. J. Geo-Inf.* **2019**, *8*, 403. [CrossRef]
25. Delchiaro, M.; Vergari, F.; Esposito, C.; Del Monte, M. The influence of anthropogenic topographic changes on geomorphological processes in the city of Rome (Italy): A case study of the Malagrotta area. *Earth Surf. Process. Landf.* **2025**, *50*, e70033. Correction in *Earth Surf. Process. Landf.* **2025**, *50*, e70056. [CrossRef]
26. Geological Map of Spain, Sheets 925 and 18-37 (1972), Instituto Tecnológico GeoMinero de España (IGME), 1:50 000 Scale. Available online: https://info.igme.es/catalogo/resource.aspx?portal=1&catalog=3&ctt=1&resource=7029&lang=eng&dlang=eng&llt=dropdown&q=puntos%20de%20agua&master=infoigme&shpu=true&shcd=true&shrd=true&shpd=true&shli=true&shuf=true&shto=true&shke=true&shla=true&shgc=true&shdi=true (accessed on 18 October 2026).
27. Spanish Ministry for Ecological Transition and Demographic Challenge, Spanish Ministry of Transport and Sustainable Mobility. Available online: https://transparencia.gob.es/en/publicidad-activa/por-materias/organizacion-empleo/funciones/funciones-mted (accessed on 18 October 2026).
28. Chen, Y.-C. High-Resolution Monitoring of Badland Erosion Dynamics: Spatiotemporal Changes and Topographic Controls via UAV Structure-from-Motion. *Water* **2026**, *18*, 234. [CrossRef]
29. Soriano, M.-A.; Álvarez, S.; Landa, B.B.; Gómez, J.A. Soil properties in organic olive orchards following different weed management in a rolling landscape of Andalusia, Spain. *Renew. Agric. Food Syst.* **2014**, *29*, 83–91. [CrossRef]
30. Ezeh, C.; Preko, K.; Igwe, O.; Adjei, K.; Schönbrodt-Stitt, S.; Asare, M.Y. Assessment of gully erosion: A review. *Parana J. Sci. Educ.* **2021**, *7*, 251–275. Available online: http://tiny.cc/PJSE24476153v7i6p251-275.
31. Anders, N.S.; Seijmonsbergen, A.C.; Bouten, W. Multi-scale and object-oriented image analysis of high-res LiDAR data for geomorphological mapping in Alpine mountains. In Proceedings of the Geomorphometry, Zurich, Switzerland, 31 August–2 September 2009.
32. Conoscenti, C.; Rotigliano, E. Predicting gully occurrence at watershed scale: Comparing topographic indices and multivariate statistical models. *Geomorphology* **2020**, *359*, 107123. [CrossRef]
33. Lima, F.; Blanco-Sepúlveda, R.; Gómez-Moreno, M.L.; Dorado, J.; Peña, J.M. Mapping tillage direction and contour farming by object-based analysis of UAV images. *Comput. Electron. Agric.* **2021**, *187*, 106281. [CrossRef]
34. Pantazis, C.; Nastos, P.T. Land Degradation Assessment in an Olive Orchard Using Different Soil Erosion Estimation Methods. *Land* **2026**, *15*, 794. [CrossRef]
35. Poesen, J.; Nachtergaele, J.; Verstraeten, G.; Valentin, C. Gully erosion and environmental change: Importance and research needs. *Catena* **2003**, *50*, 91–133. [CrossRef]
36. Milan, D.J.; Heritage, G.L.; Large, A.R.G.; Fuller, I.C. Filtering spatial error from DEMs: Implications for morphological change estimation. *Geomorphology* **2011**, *125*, 160–171. [CrossRef]

37. Gómez, J.A.; Guzmán, G.; Giráldez, J.V.; Vanwalleghem, T. Gully erosion control techniques. In *Best Management Practices for Soil and Water Conservation in Mediterranean Agriculture*; Digital CSIC: Madrid, Spain, 2021; pp. 51–58.
38. Queensland Government. Gully erosion and its control. In *Soil Conservation Guidelines for Queensland*; Department of Environment and Science: Victoria, BC, Canada, 2019; Chapter 13, pp. 1–12.
39. Natural Resources Conservation Service. *Controlling Ephemeral Gullies: Conservation Practices for Highly Erodible Land*; United States Department of Agriculture: Washington, DC, USA, 2018.

Disclaimer/Publisher's Note: The statements, opinions and data contained in all publications are solely those of the individual author(s) and contributor(s) and not of MDPI and/or the editor(s). MDPI and/or the editor(s) disclaim responsibility for any injury to people or property resulting from any ideas, methods, instructions or products referred to in the content.